# Current status and development of CMOS SiPM for scintillator-based radiation detectors toward all-digital sensors [Invited]

Nicola D'Ascenzo[1,2*], Wentao Hu (胡文韬)[1,2], Hui Lao (劳 慧)[3], Yuexuan Hua (华越轩)[3], Bo Zhang (张 博)[1,4], Lei Fang (房 磊)[1,4], Daoming Xi (奚道明)[5], Rui Zheng (郑 睿)[6], Ao Qiu (邱 奥)[1,2], Emanuele Antonecchia[1,2], Yiqing Ling (凌怡清)[1,2], Yuqing Liu (刘雨晴)[6], Yan Li (李 琰)[7], Hang Yu (俞 航)[7], Peng Xiao (肖 鹏)[1,2], and Qingguo Xie (谢庆国)[1,2**]

[1] Wuhan National Laboratory for Optoelectronics, Wuhan 430074, China
[2] Biomedical Engineering Department, Huazhong University of Science and Technology, Wuhan 430074, China
[3] RAYQUANT Technology Co., Ltd., Ezhou 436044, China
[4] RAYSOLUTION Healthcare Co., Ltd., Hefei 230000, China
[5] RAYMEASURE Technology Co., Ltd., Suzhou 215000, China
[6] RAYCAN Technology Co., Ltd., Suzhou 215000, China
[7] College of Computer Science and Software Engineering, Shenzhen University, Shenzhen 518060, China

*Corresponding author: ndasc@hust.edu.cn
**Corresponding author: qgxie@hust.edu.cn

Modern scintillator-based radiation detectors require silicon photomultipliers (SiPMs) with photon detection efficiency higher than 40% at 420 nm, possibly extended to the vacuum ultraviolet (VUV) region, single-photon time resolution (SPTR) < 100 ps, and dark count rate (DCR) < 150 kcps/mm$^2$. To enable single-photon time stamping, digital electronics and sensitive microcells need to be integrated in the same CMOS substrate, with a readout frame rate higher than 5 MHz for arrays extending over a total area up to 4 mm × 4 mm. This is challenging due to the increasing doping concentrations at low CMOS scales, deep-level carrier generation in shallow trench isolation fabrication, and power consumption, among others. The advances at 350 and 110 nm CMOS nodes are benchmarked against available SiPMs obtained in CMOS and commercial customized technologies. The concept of digital multithreshold SiPMs with a single microcell readout is finally reported, proposing a possible direction toward fully digital scintillator-based radiation detectors.

## 1. Introduction

The silicon photomultiplier (SiPM) is an array of single-photon sensing microcells operated in Geiger mode. It has emerged as one of the key photodetectors for photonics applications and optoelectronics, due to its compact size of few mm$^2$, high gain obtained with a bias voltage of few tens of volts, and high sensitivity to single photons[1–3]. Current commercial SiPMs developed with customized silicon processes reached state-of-the-art performance, with dark count rate (DCR) lower than 50 kcps/mm$^2$ (cps, counts per second), photon detection efficiency (PDE) higher than 45% at 420 nm and 20% at 905 nm, substituting the traditional photomultiplier tubes not only in scintillator-based radiation detectors for nuclear medicine, particle physics, and security systems, but also in communication and automotive devices[4–6].

Unfortunately, these commercial customized SiPMs are analog sensors, based on the parallel readout of the array of microcells. They cannot exploit the space–time patterns of correlated optical photons fluxes, which are expected to open a new approach to digital signal processing in scintillator-based radiation detectors, improving timing and spatial localization[7]. In order to form a digital pulse for each detected photon and to provide a time stamp with a precision of a few picoseconds, dedicated digital electronics can be implemented on-chip, requiring the challenging fabrication of the high electric field SiPM

detection structures and transistor-based digital electronics in the same complementary metal-oxide semiconductor (CMOS) process.

This review is organized as follows. In Section 2 we outline the basic concepts of the SiPM working principle and we describe the key performance indicators, which will be used to benchmark CMOS SiPMs. In Section 3 we report the SiPM requirements for application to scintillator-based radiation detectors. In Section 4 we review the achieved performance of CMOS SiPMs and we compare them with custom-based available commercial technologies. Finally, in Section 5 we exploit the transition to digital SiPM technologies, and we describe the new concept of multithreshold SiPMs (MT-SiPMs).

## 2. SiPM Working Principle and Benchmarking

### 2.1. SiPM: an intrinsically digital device

The basic detection structure of a SiPM, called a microcell, is shown in Fig. 1(A). It consists of a $p^+/n$ or $n^+/p$ junction operated in reverse mode with a bias $V_b$ exceeding up to 10 V, the breakdown voltage $V_{break}$. A lowly doped guard ring surrounds the junction and guarantees the uniformity of the electric field at the doping discontinuities. The attenuation of the electric field strength can also be achieved with other guard ring structures, such as virtual guard rings. The typical size of a microcell ranges between $10\,\mu m \times 10\,\mu m$ and $100\,\mu m \times 100\,\mu m$.

The working principle of the SiPM can be summarized as the sequence of three states, each characterized by a physical and electronic process. These states can be better explained in the current-voltage ($I$–$V$) graphics, as shown in Fig. 1(B). When the SiPM is biased at $V_b$ exceeding $V_{break}$, the capacitance $C_{microcell}$ formed in the $p^+/n$ junction is charged. This stable state (1) can be interrupted only when an electron/hole pair is formed within the junction, either through thermal excitation and intraband tunneling, or through the detection of an optical

photon via photoelectric interaction. The electric field in the junction reaches values up to $10^5$ V/cm, enough to accelerate both electrons and holes to the kinetic energy above the threshold for the impact-ionization process. This mechanism induces an uncontrollable avalanche and brings the junction to the breakdown state (2). Each microcell is equipped with a quenching element. In case of passive quenching, a resistor with values ranging between 50 kΩ and 500 kΩ is placed in a series to each microcell. The resistor causes a voltage drop, lowering the voltage at the diode below $V_b$, quenching the avalanche and bringing the SiPM to the recovery state (3). Within a relaxation time of few nanoseconds, the capacitance charges back to the stable state (1). Similarly, active quenching circuits act as an avalanche-sensing switch, turning off the device and bringing the SiPM from the state (3) to the state (1) within a fast time.

The sequence of SiPM states generates an electronic pulse, which is shown in Fig. 1(C). It is characterized by a fast rising component, corresponding to the avalanche generation and propagation in the junction, followed by a slower decay component determined by the characteristic recovery time of the junction. The rising time is defined by the generation time of the avalanche breakdown process and is characterized by the drift time of carriers under the high electric field. The drift velocity of the carriers under an electric field of about $10^5$ V/cm is limited by the scattering process and in silicon structures is approximately $10^7$ cm s$^{-1}$. As an example, the rising time is about 10 ps for a 1 μm-thick depleted junction.

The SiPM is therefore an intrinsically digital sensor, able to produce a single and visible fast electric pulse in correspondence to a single detected optical photon. However, the digital nature of SiPMs has not been fully exploited, and the currently available devices are analog. They consist of an array of microcells with parallel readout, the output signal being the sum of the analog signals of each microcell[2]. The frontier of SiPM, however, is represented by digital devices, with readout electronics on-chip, providing the time stamp of each detected optical photon in each microcell[7].

The transition from analog to digital SiPMs requires the development of dedicated transistor-based digital readout electronics on-chip for each microcell[8]. This is possible only if both the SiPM microcells and the transistor-based digital readout electronics are manufactured in a CMOS process[9–11]. This observation opens the challenging problem of realizing a SiPM microcell in CMOS with performance at least equivalent to the competitive commercial devices obtained with custom-based and specialized non-CMOS-compatible processes.

### 2.2. SiPM benchmarking parameters

A set of parameters has been selected to benchmark a SiPM technology in the context of radiation sensors and is used in order to compare CMOS-based and custom-technology-based sensors[12]. The gain is the number of avalanche electrons produced in correspondence to the detection of a single optical photon. The DCR is the number of electron/hole pairs generated per time unit by either thermal excitation or intraband tunneling
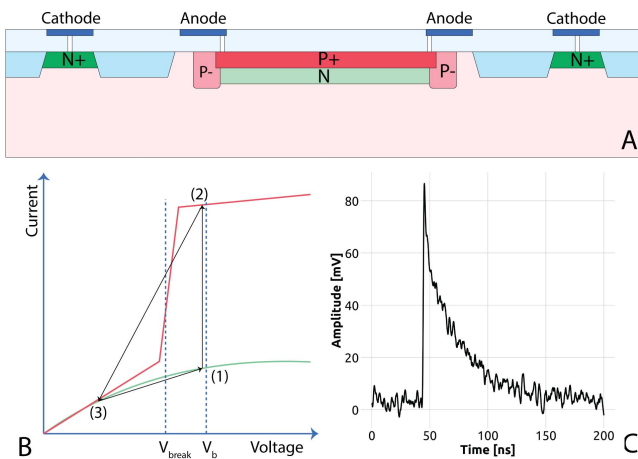


**Fig. 1.** (A) Schematic of general structure of a SiPM microcell; (B) working principle of the SiPM; and (C) pulse shape corresponding to a single detected optical photon.

and triggering an avalanche signal. The PDE is the detection probability of an optical photon. It is defined as

$$\text{PDE} = \eta(\lambda) \times P_b(V) \times \text{FF}, \tag{1}$$

where $\eta$ is the quantum efficiency of the SiPM microcell, $P_b(V)$ is the voltage-dependent probability of the avalanche breakdown in the silicon structure, and FF is the geometrical fill factor of the device, which includes the nonsensitive areas covered by metal and supporting electronics at the surface of the SiPM. The single-photon time resolution (SPTR) is the intrinsic time resolution in response to a single detected photon. It is mainly affected by the rising time of the avalanche breakdown signal. The cross talk (CT) is the probability that optical photons generated through intraband electron–phonon scattering during the avalanche process in a microcell are detected in nearby cells, therefore increasing the total number of effective detected optical photons.

The optimal value of these parameters depends on the application and defines the suitability of CMOS processes for a specific SiPM design and fabrication. The selection of a CMOS node depends in fact on the target value of the SiPM benchmark parameters to be achieved. In the following sections, the specific requirements set by SiPM-based scintillation radiation detectors enabled by the modern frontier of spatiotemporal digital signal processing and the corresponding challenges set by the limitations of CMOS processes will be reviewed.

## 3. Theoretical Basis of Single-Photon Spatiotemporal Digital Signal Processing for Scintillator-Based Radiation Detectors and SiPM Requirements

### 3.1. Physics of scintillation optical photon production, transport, and detection

In order to define the set of benchmarking parameters of the SiPM suited to scintillator-based radiation detectors, it is necessary to shortly review the basic physical mechanisms occurring in the detection of particles in scintillator/SiPM radiation detectors. An overview of the detection mechanisms and further signal generation is shown in Fig. 2. Radiation detection in scintillation-based detectors consists of two steps. First, the energy of elementary particles is converted into scintillation optical photons. Second, the scintillation optical photons are detected in a sensor and generate an electronic signal, which is further elaborated with digital signal processing techniques[13,14]. γ-rays below approximately 2 MeV release their energy to a single electron in the scintillator, mainly through photoelectric and Compton interaction. Higher energy γ-rays also undergo pair production. Charged particles release their energy to atomic electrons mainly through the ionization process. In organic scintillators, the main conversion energy is luminescence from singlet–singlet relaxation. In the crystalline structure of inorganic scintillators, excited electrons in the valence band reach an intermediate excited state formed by impurities in the crystal lattice. The de-excitation to the valence energy band produces a single optical photon. The typical
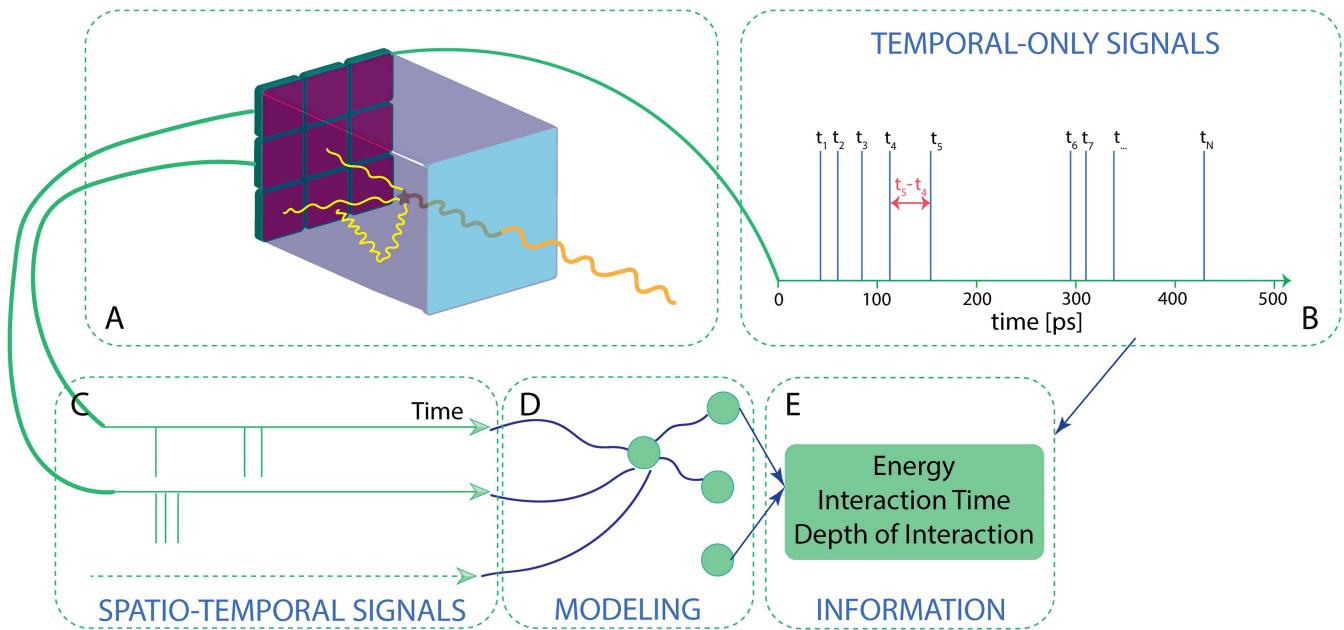


**Fig. 2.** (A) The SiPM is an intrinsically digital technology. When a particle (here a γ-ray as an example) is detected in the scintillator, scintillation optical photons are produced. They are detected in the microcells composing the SiPM. (B) Each detected optical photon generates a signal. The time sequence of all signals generates a temporal-only digital signal, which can be analyzed to extract energy, interaction time, and depth of interaction information. (C)–(E) The time sequence of the signals for each microcell generates a spatiotemporal series of digital signals, which can be modeled to extract with higher precision the information about the interaction of the primary particle.

number of scintillation photons produced by modern scintillating crystals is about 1 photon/keV and 30 photons/keV in organic and inorganic scintillators, respectively[15]. The emission time of these scintillation optical photons follows a typical exponential decay distribution, with characteristic time up to a few tens of nanoseconds. Scintillators emit visible light with a broad spectrum that extends in the ultraviolet (UV) range. For instance, BGO, LSO:Ce, and NaI:Tl emission peaks are at 480, 420, and 415 nm, respectively.

Recently, Cherenkov emission has been considered also for fast radiation detector applications[16]. This process consists of the emission of prompt optical photons, when the electron released after radiation detection moves faster than light in the medium. For instance, a few tens of Cherenkov optical photons are emitted in BGO after the detection of a 511 keV γ-ray. They have a broad spectrum, with wavelength extending below 350 nm.

As represented in Fig. 2(A), scintillation and Cherenkov optical photons undergo a series of transport processes from the emission site in the crystal to the photodetector. They can be reflected, refracted, or absorbed at crystal surfaces and absorbed or scattered in the crystal bulk. Rayleigh scattering by particles much smaller than the wavelength of the scintillation light is typically negligible[17].

Optical photons are finally detected at the photodetector via photoelectric effect and produce an electronic pulse, which is further collected and analyzed. They are emitted within few micrometers from the radiation detection site, and are therefore correlated in space and time. However, transport mechanisms alter this correlation and have an impact on the distribution in space and in time at the photodetector. The observation of the space–time signal generated by the optical photons detected at the photodetector sets the stringent requirements to the benchmarking parameters of the SiPM, which are summarized in Table 1 and are reviewed below. It is important to note that these benchmarking parameters need to be obtained at the same excess bias voltage.

**Table 1.** Summary of SiPM Requirements for Scintillator-Based Radiation Detectors.

| Observable | Parameter | Value |
|---|---|---|
| Integral | PDE | > 40%@420 nm |
|  | PDE | Extended below 350 nm |
| Temporal | SPTR | < 100 ps |
|  | PDE | > 40%@420 nm |
|  | DCR | < 150 kcps/mm$^2$ |
| Spatiotemporal | Frame rate | > 5 MHz for 4 mm × 4 mm |
|  | Microcell pitch | < 50 μm |

## 3.2. SiPM requirements from integral observables

The total number of detected scintillation optical photons in the SiPM $N_\gamma$ is proportional to the energy deposited by the elementary particle in the scintillator, according to the relationship

$$N_\gamma = \text{LY} \times \text{PDE} \times E_\gamma \times \varepsilon_{\text{opt}}, \qquad (2)$$

where LY is the light yield of the scintillator and $\varepsilon_{\text{opt}}$ is the scintillator light transport efficiency. The energy resolution (FWHM) of a scintillator/photodetector system is[15]

$$R_E(\text{FWHM}) = 2.35\frac{\sigma}{E} = 2.35\sqrt{\frac{\sigma_{\text{intr}}^2}{E_\gamma^2} + \frac{1}{\text{LY} \times \text{PDE} \times E_\gamma \times \varepsilon_{\text{opt}}}}, \qquad (3)$$

where $\sigma_{\text{intr}}$ in the first term includes the intrinsic fluctuation of the scintillation emission and the second term reflects the Poisson nature of the counting statistics.

In correspondence to a 511 keV γ-ray detected in an LYSO crystal, approximately 13,000 scintillation optical photons are produced. Following Eq. (3), an average PDE above approximately 40% is needed in the scintillation emission spectral range peaking at 400–420 nm to limit the statistical fluctuation contribution below 4%–5%. This requirement is more stringent for the detection of radiation with lower energy. As for Cherenkov emission detection, the small number of optical photons needs a high PDE below 350 nm.

## 3.3. SiPM requirements from temporal observables

As shown in Fig. 2(B), the scintillation optical photons produced after the interaction of a particle in a scintillator are detected in the SiPM array and generate a series of electronic pulses in time. When the pulses are collected in sequence, independently on the generating microcell, a temporal-only signal is produced.

The most important parameter to be estimated from the time series is the detection time of the primary particle. Due to the intrinsic noise, the best approximation to the interaction time is not necessarily the first detected optical photon. Advanced digital signal processing applied to the time series allows the extraction of precise timing information and even more parameters. It has been reported that algorithms based on the multiple time differences between the single-photon time stamps, kernel density estimation nonparametric analytical PDF extraction techniques, and neural network approaches act as a filter for the extraction of the radiation detection time and may allow the identification of the interaction position of the radiation in 2 mm × 2 mm × 20 mm and 3 mm × 3 mm × 20 mm scintillators[7].

However, both the transport mechanisms and the SiPM properties include a significant jitter in the detection time of the first optical photon. As for the detector, reflections at the crystal surfaces randomly affect the path length, and therefore the optical photons' arrival time at the SiPM surface. As for the SiPM, three parameters contribute to the timing. First, the SPTR affects the

intrinsic jitter of the single-photon time signal. Its contribution needs to be minimized to less than 100 ps for sensors with areas between 3 mm × 3 mm and 4 mm × 4 mm, in order to be compatible with the intrinsic time response of the SiPM. Second, the PDE affects the probability of detection of the single photon. It has been estimated that it deteriorates from 8 to 190 ps when the average PDE decreases from 57% to 5%[13]. Therefore, the stringent limit to the PDE reported for the integral observables also has a direct implication in the time resolution. Third, the DCR generates spurious signals, which mimic the single-photon detection and are an irreducible background for the identification of the first detected photon. In order to reduce the contribution of the DCR, a stringent limit is required. With reference to the typical scintillation pulse length of 200 ns, 0.5 dark pulses in a total maximal area of 16 mm$^2$ represent a safe limit below the single-photon timing threshold and reduce baseline fluctuations. This results in a DCR lower than approximately 150 kcps/mm$^2$.

### 3.4. SiPM requirements from spatiotemporal observables

The frontier of radiation detector technology is, however, the availability of the space–time information of the detected optical photons at the SiPM. As shown in Figs. 2(C)–2(E), when the pulses corresponding to the optical photon detection are collected for each microcell separately, the output of the SiPM is an array of digital signals, which represents the complete information of the scintillation photon flux generated by the primary particle.

Clearly, processing the time stamp of each single detected photon would not be feasible in large-scale applications. Therefore, following the multivoltage threshold (MVT) approach[14], digital signal processing methods involving space–time undersampling are currently under investigation to reduce the space–time information to the minimal requirement for further reconstruction. This theoretical development represents a current open challenge in digital signal processing for modern radiation detectors.

Digital signal processing algorithms and dedicated mathematical modeling based on gradient-tree boosting and maximum likelihood techniques have shown how this approach could allow reaching detection time resolution below 200 ps and depth of interaction capability in the detection of 511 keV γ-rays in 32 mm × 32 mm × 12 mm monolithic crystals' readout by digital photon counting (DPC 3200-22, Philips)[18,19]. However, these sensors do not provide the time stamps for each detected optical photon, but only a single time for the entire sensor.

The exploration of the spatiotemporal single-photon signals with good spatial resolution requires a SiPM with a microcell pitch not larger than 50 µm to reduce pile-up and linearity losses, with single-pixel readout. Clearly, for the compactness and feasibility of the sensor, digital electronics needs to be integrated on-chip. The readout frame rate is an essential characteristic. Considering a typical scintillator emission time of 200 ns, the frame rate should be at least 5 MHz for an array covering a total area of 4 mm × 4 mm in order to be usable in the applications of scintillator-based radiation detectors. Finally, the

realization of a SiPM with integrated electronics on-chip requires the fabrication of both the sensor and the electronics readout in the same CMOS process.

## 4. Establishment of the Analog SiPM for Scintillator-Based Radiation Detectors in a CMOS Process

The realization of a digital SiPM device for radiation detectors, with electronics integrated on each microcell, requires the preliminary challenging step of identifying a suitable CMOS technology for the implementation of the SiPM microcell detection structure. It is therefore necessary to produce an analog CMOS SiPM and benchmark it against customized available commercial SiPMs. The CMOS technology with the most competitive outcome can be selected for further implementation of on-chip electronics. The challenges and characterization of CMOS SiPMs obtained at the 350 and 110 nm CMOS nodes are reported below, benchmarked against customized commercial technologies and other CMOS nodes.

### 4.1. DCR

#### 4.1.1. State of the art in customized and CMOS-based technologies

Spurious pulses mimicking the detection of single photons are caused by trap-assisted thermal carrier generation, band-to-band tunneling, and trap-assisted tunneling and excitonic generation. Two main problems affect the DCR of SiPM structures manufactured in a CMOS process. First, when scaling down the technology node, the doping concentration increases, with a consequent increment of the tunneling noise. Second, shallow trench isolation (STI) is automatically formed between p$^+$ and n$^+$ layers in order to isolate each transistor. However, the STI fabrication process causes a significant rise in the density of deep-level carrier generation centers at its interface and therefore worsens the DCR performance of the sensor[20].

Customized technologies have the advantage of freely adapting the fabrication processes to reduce the DCR. They therefore set the lower limits to the achievable DCR in SiPM detection structures. The SiPMs produced by OnSemi (C-SERIES) exhibit a DCR ranging between 30 kcps/mm$^2$ and 96 kcps/mm$^{2[4]}$. Similarly, the SiPMs produced by Hamamatsu have an average DCR of approximately 60 kcps/mm$^{2[5]}$. The technology proposed by Broadcom has a slightly higher DCR of approximately 125 kcps/mm$^2$ (AFBR-S4N44P044M-2x2-NUV-MT)[6,8,21].

As represented in Fig. 3(A), the performance of single-photon avalanche structures fabricated within a CMOS process has a large variation, which is well above the benchmarking limit set by customized technologies. Most of the cited results refer to single-photon avalanche diodes (SPADs) realized in CMOS processes, which have the same detection structure as SiPM microcells and can be used to benchmark in terms of DCR the feasibility of CMOS processes for the fabrication of SiPMs.

Several structures have been realized in an 800 nm CMOS technology, with a DCR ranging between 140 kcps/mm$^2$ and
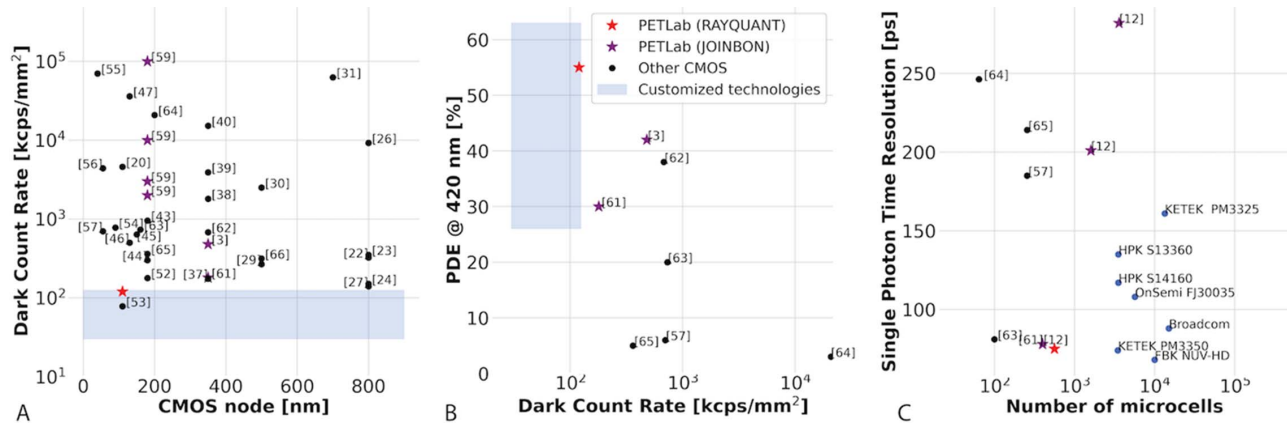
**Fig. 3.** Characterization of CMOS SiPMs. (A) DCR of SPADs and SiPMs obtained in standard CMOS technology nodes; (B) PDE; and (C) SPTR versus number of microcells of available CMOS SiPMs. The shaded area in (A) and (B) is covered by customized commercial technologies and represents the benchmark target of CMOS SiPMs.

$62.5\,MHz/mm^2$[22–28]. As expected, at smaller technology scales, the DCR tends to increase. The best SiPM produced at a 500 nm CMOS node has a DCR of $500\,kcps/mm^2$[29]. Other single-photon avalanche structures produced at 500 and 700 nm CMOS nodes experience a higher DCR[30,31]. The 350 nm CMOS node has been extensively exploited[32–41], and improvements in the fabrication processes, also thanks to the development of CMOS-compatible specialized doping layers specifically tuned to the SiPM requirements, have reached a competitive DCR of $175\,kcps/mm^2$[37] at smaller scales, between 130 and 200 nm[42–52]. SiPM detection structures were also developed at 110[20,53], 90[54,55], 55[56], 45[57], and 40 nm[58] CMOS technology nodes. Among them, the detection structure produced at the Dongbu 110 nm CMOS node exhibited a DCR as low as $78\,kcps/mm^2$, therefore being competitive with commercial customized technologies[53].

### 4.1.2. CMOS SiPM advances at 350 and 110 nm

The research of the PETLab group aimed at finding a CMOS node with a scale as low as possible, but still allowing a competitive DCR with respect to customized technologies. One of the first tested options was the BCDLite 180 nm CMOS process (GLOBALFOUNDRIES)[59,60]. As expected, when STI was formed in the vicinity of the high-field detecting structure, the DCR reached a value of $2 \times 10^4\,kcps/mm^2$. When the STI was produced at a distance from the sensitive area, by using a poly layer, the best obtained DCR value was $3 \times 10^3\,kcps/mm^2$. As is visible in Fig. 3(A), these results confirmed other studies performed at 180 nm CMOS nodes and supported the evidence that STI needs to be controlled when producing a SiPM in a standard CMOS process.

Modern CMOS nodes offer the possibility of customized layers with user-defined doping concentrations and profiles, compatible with the underlying CMOS process. This option enables the design of the SiPM detecting structures without affecting the layers dedicated to transistors. The PETLab group

tested this option at a 350 nm node first[3,12,61]. As shown in Fig. 3(A), the best obtained DCR was $180\,kcps/mm^2$, confirming previous studies[37]. However, the devices were not yet competitive with respect to customized technologies. The 110 nm CMOS node currently offers the best platform for the realization of the SiPM detecting structures. The PETLab group has recently obtained a 110 nm CMOS SiPM with an average DCR of $120\,kcps/mm^2$, competitive with existing custom devices (RAYQUANT Technology Ltd.). While previous studies were focusing on single SPADs[53], the PETLab group demonstrated the feasibility of a 110 nm CMOS node to the stable fabrication of a complete SiPM. This is the only SiPM produced at a CMOS node and with a DCR competitive with existing custom technologies.

### 4.2. PDE

#### 4.2.1. State of the art in customized and CMOS-based technologies

The key factors affecting the PDE of a SiPM follow from Eq. (1). First, $\eta(\lambda)$ at a certain wavelength is determined by the depth of the sensitive region. The absorption coefficient of silicon at 420 nm and room temperature is $5 \times 10^4\,cm^{-1}$. Therefore almost 40% of a 420 nm photon flux is absorbed within just $0.2\,\mu m$ silicon depth. This implies that a SiPM developed for scintillator-based radiation detectors should have a sensitive area as shallow as possible. However, $SiO_2$ isolation and metal layer deposition at the surface may generate local impurities, which may cause high DCR generation. Second, due to the difference in refraction index between the air and the $SiO_2$ isolation layer, a fraction of the incident optical photons are reflected at the surface of the sensor. Third, FF depends on the electronics components that are contained in a microcell, on the guard ring structure, and on the minimally allowed distance between microcells. A small CMOS scale is therefore preferable, although, as mentioned above, it implies higher DCR.

As represented in Fig. 3(B), the trade-off between PDE and DCR is a challenging issue in the fabrication of CMOS

SiPMs. The performance of a SiPM obtained with customized technologies sets the benchmark limits to CMOS SiPMs. Hamamatsu, OnSemi, and Broadcom reach a PDE of 40%, 41%, and 63% at 420 nm, respectively[4–6].

When it comes to CMOS SiPMs, few examples of fully characterized analog sensors are available. In fact, single CMOS SPADs cannot be considered for the analysis of the achievable PDE in CMOS SiPMs, due to the intrinsic difference in filling factor. Two devices realized, respectively, at 350 and 160 nm represent the best possible improvement for radiation detectors. At the 350 nm CMOS node, a SiPM composed of an array of $16 \times 16$ 58 µm pitch microcells with a total active area of $928\,\mu m \times 928\,\mu m$ has been reported, reaching a PDE of 38% at 420 nm and a DCR of 680 kcps/mm$^2$[62]. Finally, a SiPM fabricated in the 160 nm BCD (bipolar-CMOS-DMOS) technology, with 0.67 mm $\times$ 0.67 mm total area, formed by $10 \times 10$ square pixels and with a 53% FF has been reported with a PDE of 20% at 420 nm and a DCR of 732 kcps/mm$^2$[63]. As is visible in Fig. 3(B), the three devices are not competitive with respect to custom technologies. However, these results demonstrate the possibility of realizing a complete analog SiPM in a CMOS production line.

The development of a CMOS SiPM continues to be driven by automotive applications. This explains why many existing attempts have a PDE optimized for higher wavelengths. For instance, in a 55-nm standard BCD technology, a SiPM composed of an array of $16 \times 16$ microcells, based on a deep-p-well/buried-n-well (DPW/BNW) junction, has been reported with a PDE of 11% at 550 nm, which could be enhanced with the use of microlenses. The depth of the junction reduces the PDE at 420 nm to approximately 6%. The DCR of the device was 700 kcps/mm$^2$[57]. Similarly, at a LAPIS Semiconductor 200 nm five-metal SOI-CMOS technology, an SOI-SiPM composed of $8 \times 8$ microcells, with integrated electronics, exhibited a PDE of 8.1% at 550 nm, with a DCR of 20.8 MHz/mm$^2$[64]. At a 180 nm HV CMOS node, a SiPM composed of 256 microcells based on a p-well/deep n-well junction was adopted. The depth of the junction was optimized for the longer wavelength region, reaching a peak PDE of 29.5% at 600 nm. With low doping levels, the avalanche multiplication region was wider, and the DCR contributed by band-to-band tunneling could be reduced, leading to a DCR of 361 kcps/mm$^2$. However, the PDE at 420 nm was approximately 2%[65]. Finally, in a 500 nm 2-poly and 3-metal CMOS process, an $18 \times 18$ pixels analog perimeter-gated-based CMOS SiPM has been reported with a peak PDE of 6.11% at 470 nm–estimated from the QE and filling factor–and DCR of 314 kcps/mm$^2$[66]. When exported to a digital $4 \times 4$ pixel array, the same technology resulted in a peak PDE of 35% at 500 nm with a DCR of 267 kcps/mm$^2$. The PDE at 420 nm, however, dropped significantly[29].

### 4.2.2. CMOS SiPM advances at 350 and 110 nm

As in the case of the DCR improvement mentioned above, the availability of customized doping masks within standard CMOS processes was the key factor for the development of the high-PDE CMOS SiPMs by the PETLab group. The first analog CMOS SiPM developed by the HUST team was at a 350 nm CMOS node, providing four metal layers, two polysilicon layers, high-resistance polysilicon, and two types of transistor gates (3.3 and 5 V)[61]. A p$^+$/n well junction was obtained with an n-enrichment implantation in the standard CMOS n-well. Light-doped p-type guard rings were used to prevent localized breakdown at the edges of the diode. The size of a sensitive cell was 50 µm $\times$ 50 µm. CMOS SiPMs with area 1 mm$^2$, 4 mm$^2$, and 9 mm$^2$ and number of cells $20 \times 20$, $40 \times 40$, and $60 \times 60$, respectively, were fabricated. The cells had a common anode and cathode within a common n-well realized in a p-doped substrate[12]. The peak PDE of 35% 420 nm was obtained with a DCR, as mentioned above, of approximately 180 kcps/mm$^2$. This process resulted in the CMOS SiPM JSP commercial product lines (JOINBON)[67]. Some of the commercially available CMOS SiPMs, also fabricated in packaged arrays, are shown in Fig. 4.

The junction depth at approximately 0.3 µm impaired the PDE at the UV range. As a next step, a shallow-junction CMOS SiPM was produced with the same 350 nm CMOS technology. The CMOS SiPM was composed of an array of $20 \times 20$ shallow junction microcells with size 50 µm $\times$ 50 µm. The p$^+$/n junction was at a depth of 0.13 µm and enabled a peak PDE of 41% at 420 nm. An antireflecting coating (ARC) optimized for 420 nm optical photons improves the peak PDE up to 42% at 420 nm[3]. However, surface impurities during the processing increased the DCR up to 480 kcps/mm$^2$. These results indicated that a shallow junction is needed for CMOS SiPM optimized for radiation detectors. Moreover, a limitation of the 350 nm CMOS technology was the minimal distance between microcells, which could not be kept lower than approximately 1.5 µm, leading to a fill factor never better than approximately 68%. This observation brought the PETLab group to consider smaller scales.

Recently, the PETLab group realized a 1 mm$^2$ CMOS SiPM with 35 µm pixels (RAYQUANT) in a 110 nm CMOS process. The shallow-junction process and the minimal separation between microcells due to the smaller scale allowed the group to reach a PDE of approximately 55% at 420 nm, with a DCR of 120 kcps/mm$^2$, as mentioned above. These are by far the best results achieved for a CMOS SiPM, competitive with respect to custom technologies.
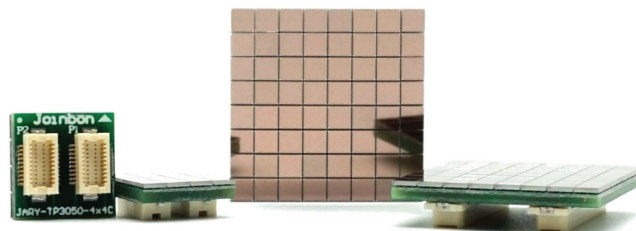


**Fig. 4.** CMOS SiPM developed at a 350 nm technology and currently commercialized also in arrays (TN and TP series, JOINBON).

### 4.3. SPTR

#### 4.3.1. State of the art in customized and CMOS-based technologies

Two factors mainly affect the SPTR of an analog SiPM. First, the doping profile and the resulting electric field. As mentioned above, the SPTR is related to the crossing time of the avalanche in the junction; therefore a high electric field distributed in a thin avalanche region is preferable. Second, the uniformity of the microcells. The SPTR is the result of the detection of a single optical photon in one of the microcells, and slight differences in the doping profiles may affect the time jitter of the device. It was shown that the SPTR is related to the number of microcells $N_{cells}$ through the following formula[12]:

$$\text{SPTR} = \sqrt{\alpha N_{cells} + \beta N_{cells}^2}, \qquad (4)$$

where the first term represents the statistical fluctuation due to the intrinsic difference of the microcells, and the second term models the additional confusion error introduced by DCR signals misidentified as detected single photons.

As reported in Fig. 3(C), customized technologies reached state-of-the-art timing performance with large-area SiPMs[68]. The Hamamatsu SiPM with 3531 microcells has an SPTR ranging between 117 (HPK S14160) and 135 ps (HPK S13360). The Ketek SiPM exhibits an SPTR of 74 ps with 3472 microcells (PM3350), which degrades up to 161 ps when the number of microcells increases to 13,408 (PM3325). The microcells size is also halved from 50 µm to 25 µm, contributing to the deterioration of the SPTR. OnSemi (former SensL) SiPMs, with 5676 pixels, report 108 ps SPTR (FJ30035). The most performant commercial device remains the Broadcom SiPM (AFBR-S4N44C013), with an SPTR of 88 ps and 15,060 microcells, followed by FBK with an SPTR of 68 ps with approximately 10,000 microcells.

CMOS SiPMs do not perform as well as the customized devices. The above-mentioned CMOS SiPMs obtained at 160[63], 55[57], 200[64], and 180 nm[65] report, respectively, an SPTR of 81 ps at 100 microcells, 185 ps at 256 microcells, 246.3 ps at 64 microcells, and 214 ps at 256 microcells. As is visible in Fig. 3(C), their performance is still poor in comparison with customized commercial technologies.

#### 4.3.2. CMOS SiPM advances at 350 and 110 nm

As mentioned above, the PETLab group developed analog CMOS SiPMs in 350 and 110 nm technologies. As shown in Fig. 3(C), the CMOS SiPMs developed at 350 nm exhibited an SPTR ranging between 77 ps (1 mm × 1 mm) and 282 ps (3 mm × 3 mm)[3,12]. The result advanced the state-of-the-art CMOS SiPMs, producing for the first time a large-area analog CMOS SiPM, with performance exceeding the existing CMOS SiPM devices. However, with respect to custom technologies, the SPTR was still poor. At 110 nm CMOS, a 1 mm × 1 mm SiPM with 564 microcells reported an SPTR of approximately 75 ps (RAYQUANT). The scalability of this result to larger-area analog CMOS SiPMs still needs to be investigated.

### 4.4. Gain and CT

The gain of the SiPM depends on the microcell capacitance and therefore on the microcell area and pn junction width. Analog SiPMs obtained in customized technologies exhibit a gain ranging between $7 \times 10^5$[5,6] and $1.7 \times 10^6$. Similarly, analog CMOS SiPMs have been reported with gains in the same range[29,52,57,62,63,65,66]. The CMOS SiPMs developed by the PETLab team confirms this trend, with a gain ranging between $1 \times 10^6$ and $3 \times 10^6$ at the operational voltage for the 350 and 110 nm CMOS nodes[3,12]. The gain does not appear as a problem of SiPMs developed in CMOS technology, as it is related to the intrinsic characteristics of the multiplication process.

Similarly, the total CT depends mainly on the geometrical separation between the microcells. Its typical value in customized technologies ranges between 3% and 14%. The 350 and 110 nm CMOS SiPMs developed by the PETLab team confirm this value[3,12].

## 5. Transition to Digital CMOS SiPMs

The results presented above support the idea that suitable CMOS processes for the realization of SiPMs competitive with customized technologies exist. This opens the way to the integration of readout electronics in each microcell. In contrast with analog SiPMs, commercial fully digital SiPMs for scintillator-based radiation sensors do not exist, and available results mainly refer to prototypes.

### 5.1. Overview of existing digital CMOS SiPMs

Philips digital photon counting (PDPC) photodetectors were the first available products with a digitalization level on-chip. The excellent timing properties were exploited in clinical PET systems[69] and in prototypes of plant PET[70] and proton range monitoring[71] systems. The digital nature of PDPC was used to efficiently count the number of detected photons and extract a precise event time, but the access to the space–time information of each detected optical photon was not available.

The only development of a fully digital SiPM for radiation detectors has been proposed in a Teledyne-DALSA Semiconductor Inc. (TDSI) 0.8 µm CMOS process, where a 22 × 22 SPAD array with 50 µm pitch was implemented, yielding a peak PDE of 30% at 550 nm at 5 V of excess voltage[72]. Most of the digital SiPM devices, intended as large arrays of SiPM microcells with integrated electronics, providing a time stamp for each detected optical photon, were developed for automotive applications. For instance, a 256 × 128 microcell array fabricated in a 180-nm CMOS technology was allowed to reach approximately 150 kframes/s. The device has two data streams. The first is a firing map showing the location of all of the events on the array, and the second is time stamp data packets with embedded position information[73]. Similarly, Hamamatsu developed a front side illuminated (FSI) 32 × 32 SPAD array interconnected to 180 nm CMOS readout electronics using through silicon vias (TSV). 32 time-to-digital

converters (TDCs) are available for photon time stamping at each column[74]. The optimization of the TDC is at the core of modern digital sensors, due to the minimization of power consumption. For instance, a prototype of a $2 \times 8 \times 8$ microcell digital SiPM device was fabricated in a TSMC 3D stacked 45/65-nm CMOS technology, featuring back side illumination (BSI) SPAD detectors on the top tier, and a readout circuit on the bottom tier[75]. Similarly, a $256 \times 256$ microcell integrated into a 3D-stacked 90-nm 1P4M/40-nm 1P8M process was reported with a pixel-parallel multi-event TDC approach[76]. Recently, a time-gated digital SiPM with a large 8.6 mm$^2$ photosensitive area, 37% fill factor, and 300 ps gate rising edge fabricated in 0.35 µm CMOS technology for near-infrared spectroscopy has been reported[77]. However, the development of a fully digital SiPM, providing a time stamp and position at a high frame rate, remains an open challenge in sensor technologies.

## 5.2. Concept of multithreshold SiPM

To conclude this review, we report here a novel sensor concept, which follows the logic of the MVT approach[14]. The MVT method has been invented to solve the problem of large data storage in the digitization of sensor analog pulses. When using a fixed high sampling rate, an analog pulse is represented with a large number of digital samples, requiring large storage space and transmission bandwidth. It has been demonstrated that, when the physical characteristics of the pulse shape, such as rise time and decay time, are known, it is possible to represent the analog pulse with eight samples corresponding to the crossing times of four fixed amplitude thresholds. The MVT approach allows one to develop systems with high count rate performance without increasing the required readout bandwidth.

Digital SiPMs face nowadays a similar problem to the analog case. In fact, the measurement of the spatiotemporal signals shown in Fig. 1 would require time-stamping electronics for each microcell and a large bandwidth readout stream. This generates a large data volume, decreases the frame rate capability, and causes high power consumption. Following the MVT concept, the space–time undersampling possibility has been investigated. A prototype of a sensor with space–time undersampling developed at the 350 nm CMOS node is shown in Fig. 5. It consists of an array of $32 \times 32$ microcells with an active area of 50 µm $\times$ 50 µm and a dimension of 100 µm $\times$ 100 µm, equipped with a 4-bit counter. The sensor operates in self-triggering mode. Each subgroup of $2 \times 2$ microcells has a coincidence logic, which generates a time signal with an integrated TDC. If one of the subgroups detects a signal, the frame acquisition starts.

The undersampling is obtained by combining every 16 subgroups into adjacent regions of $8 \times 8$ microcells. The fastest time of the 16 subgroups is read out. Therefore, the sensor outputs the number of counts in the $32 \times 32$ microcells and the 16 fastest detection times corresponding to the $4 \times 4$ combined subgroups adjacent regions. The 4-bit counter in each microcell and the reduced number of TDC outputs increase the frame rate up to 5 MHz and decrease the data volume. The digital SiPM with
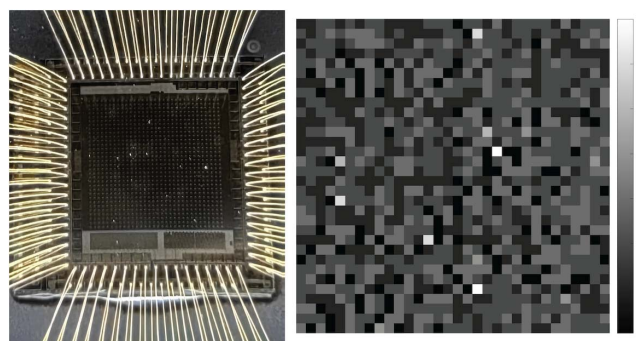


**Fig. 5.** Prototype of MT-SiPM; photo of the chip and example of detection map of a 420 nm LED photon flux with 1 kHz rate.

spatiotemporal undersampling has been called multithreshold (MT) SiPM[78].

We show here, only for sake of completeness, an example of a detection map of a photon flux in Fig. 5. The optical and dynamic characterization of this new device and the proof of concept in the readout of scintillators still needs to be completed for a demonstration that space–time undersampling can still preserve the key physical features of scintillation light needed in scintillator-based radiation detectors.

## 6. Conclusions

The 110 nm CMOS technology node offers a platform for the realization of SiPMs satisfying the requirements of radiation detectors. It has been demonstrated that a PDE of 55% at 420 nm can be reached with an average DCR of 120 kcps/mm$^2$ and an SPTR of approximately 75 ps in a prototype of 1 mm$^2$ CMOS SiPM. These results are competitive with customized technologies and open the possibility of integration of digital electronics in SiPM microcells for radiation detectors.

The MT-SiPM space–time undersampling concept is a new promising option for single-photon space-time-enabled radiation detectors. The MT-SiPM concept allows for the reduction of the number of output channels and needed TDCs without reducing the significant information needed for the reconstruction of the space–time signal information. Further digital signal processing studies are needed to validate this concept in advanced applications, such as positron emission tomography (PET).

Even in case of the MT-SiPM, the electronics required for each microcell significantly affect the fill factor. Therefore, the development of MT-SiPM will require an FSI CMOS process with 3D stacking, which leaves the sensors at the front layer and places the pixel readout electronics at a second layer.

# References

1. D. J. Herbert, V. Saveliev, N. Belcari, *et al.*, "First results of scintillator readout with silicon photomultiplier," IEEE Trans. Nuc. Sci. **53**, 389 (2006).
2. M. Bisogni, A. Del Guerra, and N. Belcari, "Medical applications of silicon photomultipliers," Nucl. Instrum. Met. Phys. Res. A **926**, 118 (2019).
3. N. D'Ascenzo, E. Antonecchia, A. Brensing, *et al.*, "A novel high photon detection efficiency silicon photomultiplier with shallow junction in 0.35 µm CMOS," IEEE Elecron. Dev. Lett. **40**, 1471 (2019).
4. https://www.onsemi.com/download/data-sheet/pdf/microc-series-d.pdf.
5. https://www.hamamatsu.com/content/dam/hamamatsu-photonics/sites/documents/99-SALES-LIBRARY/ssd/mppc-kapd0006e.pdf.
6. https://docs.broadcom.com/doc/AFBR-S4N44P044M-2x2-NUV-MT-SiPM-Array.
7. F. Loignon-Houle, S. Gundacker, M. Toussaint, *et al.*, "DOI estimation through signal arrival time distribution: a theoretical description including proof of concept measurements," Phys. Med. Biol. **66**, 095015 (2021).
8. F. Gramuglia, A. Muntean, C. Fenoglio, *et al.*, "Architecture and characterization of a CMOS 3D-stacked FSI multi-channel digital SiPM for time-of-flight PET applications," in *IEEE Nuclear Science Symposium and Medical Imaging Conference (NSS/MIC)* (2021), p. 1.
9. S. Mandai and E. Charbon, "Multi-channel digital SiPMs: concept, analysis and implementation," in *IEEE Nuclear Science Symposium and Medical Imaging Conference Record* (2008), p. 1840.
10. A. Carimatto, S. Mandai, E. Venialgo, *et al.*, "11.4 A 67,392-SPAD PVTB-compensated multi-channel digital SiPM with 432 column-parallel 48 ps 17b TDCs for endoscopic time-of-flight PET," in *IEEE International Solid-State Circuits Conference-(ISSCC) Digest of Technical Papers* (2015), p. 1.
11. L. H. C. Braga, L. Gasparini, L. Grant, *et al.*, "A fully digital 8 × 16 SiPM array for PET applications with per-pixel TDCs and real-time energy output," IEEE J. Solid-State Circ. **49**, 301 (2014).
12. X. Liang, N. D'Ascenzo, W. Brockherde, *et al.*, "Silicon photomultipliers with area up to 9 mm$^2$ in a 0.35-µm CMOS process," IEEE J. Elecron. Dev. Soc. **7**, 239 (2019).
13. N. D'Ascenzo and V. Saveliev, "Study of silicon photomultipliers for the medical imaging systems," Nucl. Instrum. Meth. Phys. Res. A **695**, 265 (2012).
14. Q. Xie, C. Kao, Z. Hsiau, *et al.*, "A new approach for pulse processing in positron emission tomography," IEEE Trans. Nuc. Sci. **52**, 988 (2005).
15. S. R. Cherry, J. A. Sorenson, and M. E. Phelps, *Physics in Nuclear Medicine* (W. B. Saunders, 2012).
16. S. Gundacker, G. Borghi, S. Cherry, *et al.*, "On timing-optimized SiPMs for Cherenkov detection to boost low cost time-of-flight PET," Phys. Med. Biol. **68**, 165016 (2023).
17. E. Roncalli, M. Mosleh-Shirazi, and A. Badano, "Modelling the transport of optical photons in scintillation detectors for diagnostic and radiotherapy imaging," Phys. Med. Biol. **62**, R207 (2017).
18. F. Müller, D. Schug, P. Hallen, *et al.*, "Gradient tree boosting-based positioning method for monolithic scintillator crystals in positron emission tomography," IEEE Trans. Rad. Plasm. Med. Sci. **2**, 411 (2018).
19. H. T. Van Dam, G. Borghi, S. Seifert, *et al.*, "Sub-200 ps CRT in monolithic scintillator PET detectors using digital SiPM arrays and maximum likelihood interaction time estimation," Phys. Med. Biol. **58**, 3243 (2013).
20. W. Ha, E. Park, B. Park, *et al.*, "Noise optimization of single-photon avalanche diodes fabricated in 110 nm CMOS image sensor technology," Opt. Express **30**, 14958 (2022).
21. G. Ambrosi, M. Ambrosio, C. Aeamo, *et al.*, "High-density near-ultraviolet silicon photomultipliers: characterization of photosensors for Cherenkov light detection," Nucl. Instrum. Methods Phys. Res. A **1049**, 168023 (2023).
22. C. Niclass, A. Rochas, P.-A. Besse, *et al.*, "Toward a 3-D camera based on single photon avalanche diodes," IEEE J. Sel. Top. Quantum Electron. **10**, 796 (2004).
23. A. Rochas, M. Gosch, A. Serov, *et al.*, "First fully integrated 2-D array of single-photon detectors in standard CMPS technology," IEEE Photon. Technol. Lett. **15**, 963 (2003).
24. S. Tisa, F. Zappa, and I. Labanca, "On-chip detection and counting of single-photons," in *IEEE InternationalElectron Devices Meeting* (2005), p. 815.
25. D. Stoppa, L. Pancheri, M. Scandiuzzo, *et al.*, "A CMOS 3-D imager based on single photon avalanche diode," IEEE Trans. Circ. Syst. **54**, 4 (2007).
26. C. Niclass, A. Rochas, P. A. Besse, *et al.*, "Design and characterization of a CMOS 3-D image sensor based on single photon avalanche diodes," IEEE J. Solid-State Circ. **40**, 1847 (2005).
27. D. Stoppa, L. Pancheri, M. Scandiuzzo, *et al.*, "A single-photon-avalanche-diode 3D imager," in *Proceedings of the 31st European Solid-State Circuits Conference* (2005), p. 487.
28. A. Rochas, M. Gani, B. Furrer, *et al.*, "Single photon detector fabricated in a complementary metal-oxide-semiconductor high-voltage technology," Rev. Sci. Instrum. **74**, 3263 (2003).
29. M. Shawkat and N. Mcfarlane, "A digital CMOS silicon photomultiplier using perimeter gated single photon avalanche diodes with asynchronous AER readout," IEEE Trans. Circ. Syst. Regul. Pap. **67**, 4818 (2020).
30. L. Pancheri and D. Stoppa, "Low-noise CMOS single-photon avalanche diodes with 32 ns dead time," in *ESSDERC 2007-37th European Solid State Device Research Conference* (2007), p. 362.
31. M. H. U. Habib and N. McFarlane, "A perimeter gated single photon avalanche diode based silicon photomultiplier as optical detector," in *IEEE 58th International Midwest Symposium on Circuits and Systems (MWSCAS)* (2015), p. 1.
32. K. Jradi, D. Pellion, and D. Ginhac, "Design, characterization and analysis of a 0.35 µm CMOS SPAD," Sensors **14**, 22773 (2014).
33. E. Vilella and A. Diéguez, "A gated single-photon avalanche diode array fabricated in a conventional CMOS process for triggered systems," Sens. Actuators A **186**, 163 (2012).
34. E. Vilella, O. Alonso, A. Montiel, *et al.*, "A low-noise time-gated single-photon detector in a HV-CMOS technology for triggered imaging," Sens. Actuator A **201**, 342 (2013).
35. A. Arbat, A. Comerma, J. Trenado, *et al.*, "High voltage vs. high integration: a comparison between CMOS technologies for SPAD cameras," Proc. SPIE **7780**, 77801G (2010).
36. D. Stoppa, D. Mosconi, L. Pancheri, *et al.*, "Single-photon avalanche diode CMOS sensor for time-resolved fluorescence measurements," IEEE Sens. J. **9**, 1084 (2009).
37. C. Niclass, C. Favi, T. Kluter, *et al.*, "Single-photon synchronous detection," IEEE J. Solid-State Circ. **44**, 1977 (2009).
38. S. Tisa, F. Guerrieri, A. Tosi, *et al.*, "100 kframe/s 8 bit monolithic single-photon imagers," in *ESSDERC 2008-38th European Solid-State Device Research Conference* (2008), p. 274.
39. S. Tisa, F. Guerrieri, and F. Zappa, "Variable load quenching circuit for single photon avalanche diodes," Opt. Express **16**, 2232 (2008).
40. C. Niclass, C. Favi, T. Kluter, *et al.*, "A 128 × 128 single-photon image sensor with column-level 10-bit time-to-digital converter array," IEEE J. Solid-State Circ. **43**, 2977 (2008).
41. C. Niclass, M. Sergio, and E. Charbon, "A single photon avalanche diode array fabricated in 0.35 µm CMOS and based on an event-driven readout for TCSPC experiments," Proc. SPIE **6372**, 63720S (2006).
42. H. Finkelstein, M. J. Hsu, and S. C. Esener, "Sti-bounded single-photon avalanche diode in a deep-submicrometer CMOS technology," IEEE Electron Dev. Lett. **27**, 887 (2006).
43. N. Faramarzpour, M. J. Deen, S. Shirani, *et al.*, "Fully integrated single photon avalanche diode detector in standard CMOS 0.18-µm technology," IEEE Trans. Electron Dev. **55**, 760 (2008).
44. L. D. Huang, J. Y. Wu, J. P. Wang, *et al.*, "Single-photon avalanche diodes in 0.18-µm high-voltage CMOS technology," Opt. Express **25**, 13333 (2017).
45. L. Pancheri and D. Stoppa, "Low-noise single photon avalanche diodes in 0.15-µm CMOS technology," in *Proceedings of the European Solid-State Device Research Conference (ESSDERC)* (2011), p. 179.
46. J. A. Richardson, L. A. Grant, and R. K. Henderson, "Low dark count single-photon avalanche diode structure compatible with standard nanometer scale CMOS technology," IEEE Photon. Technol. Lett. **21**, 1020 (2009).
47. M. Gersbach, Y. Maruyama, R. Trimananda, *et al.*, "A time-resolved, low-noise single-photon image sensor fabricated in deep-submicron CMOS technology," IEEE J. Solid-State Circ. **47**, 1394 (2012).
48. R. Henderson and L. A. Grant, "Reduction of band-to-band tunneling in deep-submicron cmos single photon avalanche photodiodes," in *International Image Sensor Workshop* (2009), p. 26.
49. C. Niclass, M. Gersbach, R. Henderson, *et al.*, "A single photon avalanche diode implemented in 130-nm CMOS technology," IEEE J. Sel. Top. Quantum Electron. **13**, 863 (2007).

50. A. Arbat, "Towards a forward tracker detector based on geiger mode avalanche photodiodes for future linear colliders," Ph.D. dissertation (University of Barcelona, 2010).
51. E. Vilella, O. Alonso, and A. Dieguez, "3D integration of geiger-mode avalanche photodiodes aimed to very high fill-factor pixels for future linear colliders," Nucl. Instrum. Methods Phys. Res. A **731**, 103 (2013).
52. A. Eshkoli and Y. Nemirovsky, "Characterization and architecture of monolithic N⁺P-CMOS-SiPM array for ToF measurements," IEEE Trans. Instrum. Meas. **70**, 2002909 (2020).
53. D. Shin, B. Park, Y. Chae, et al., "The effect of a deep virtual guard ring on the device characteristics of silicon single photon avalanche diodes," IEEE Trans. Electron Dev. **66**, 2986 (2019).
54. M. A. Karami, M. Gersbach, H.-J. Yoon, et al., "A new single-photon avalanche diode in 90 nm standard CMOS technology," Opt. Express **18** 22158 (2010).
55. E. A. Webster, J. A. Richardson, L. A. Grant, et al., "A single-photon avalanche diode in 90-nm CMOS imaging technology with 44% photon detection efficiency at 690 nm," IEEE Electron Dev. Lett. **33**, 694 (2012).
56. W. Ha, E. Park, D. Eom, et al., "Single-photon avalanche diode fabricated in standard 55 nm bipolar-CMOS-DMOS technology with sub-20 V breakdown voltage," Opt. Express **31**, 13798 (2023).
57. J. Zhao, T. Milanese, F. Gramuglia, et al., "On analog silicon photomultipliers in standard 55-nm BCD technology for LiDAR applications," IEEE J. Sel. Top. Quantum Electron. **28**, C1 (2022).
58. E. Park, W. Ha, H. Park, et al., "A back-illuminated SPAD fabricated with 40 nm CMOS image sensor technology achieving near 40% PDP at 940 nm," IEEE J. Sel. Top. Quantum Electron. **30**, 3800207 (2024).
59. N. D'Ascenzo and Q. Xie, "Possible layout solutions for the improvement of the dark rate of geiger mode avalanche structures in the GLOBALFOUNDRIES BCDLITE 0.18 µm CMOS technology," J. Instrum. **13**, T04007 (2018).
60. N. D'Ascenzo, X. Zhang, and Q. Xie, "Application of CMOS technology to silicon photomultiplier sensors," Sensors **17**, 2204 (2017).
61. N. D'Ascenzo, W. Brockherde, S. Dreiner, et al., "Design and characterization of a silicon photomultiplier in 0.35-µm CMOS," IEEE J. Elec. Dev. Soc. **6**, 74 (2018).
62. F. Villa, D. Bronzi, M. Vergani, et al., "Analog SiPM in planar CMOS technology," in *44th European Solid State Device Research Conference (ESSDERC)* (2014), p. 294.
63. M. Sanzaro, F. Signorelli, P. Gattari, et al., "0.16 µm–BCD silicon photomultipliers with sharp timing response and reduced correlated noise," Sensors **18**, 3763 (2018).
64. K. Shimazoe, C. Kim, H. Takahashi, et al., "Design improvement and characterization of SOI-based silicon-photomultiplier prototype," Nucl. Instrum. Methods Phys. Res. Sect. A **1047**, 167902 (2022).
65. M. Liu, B. Liu, J. Hu, et al., "A 16-channel analog CMOS SiPM with on-chip front-end for D-ToF LiDAR," IEEE Trans. Circuits Syst. **69**, 2376 (2022).
66. M. S. A. Shawkat, M. H. U. Habib, and N. McFarlane, "An analog CMOS silicon photomultiplier using perimeter-gated single-photon avalanche diodes," IEEE Trans. Circuits Syst. **65**, 3830 (2018).
67. N. D'Ascenzo, L. Wang, X. Zhang, et al., "The JOINBON SiPM for the read-out of LySO crystals: a multi voltage threshold approach," J. Instrum. **15**, C07006 (2020).
68. S. Gundacker, R. Turtos, N. Kratochwil, et al., "Experimental time resolution limits of modern SiPMs and TOF-PET detectors exploring different scintillators and Cherenkov emission," Phys. Med. Biol. **65**, 025001 (2020).
69. T. Frach, G. Prescher, C. Degenhardt, et al., "The digital silicon photomultiplier—principle of operation and intrinsic detector performance," in *Proceedings of the IEEE Nuclear Science Symposium Conference Record* (2009), p. 1959.
70. M. Streun, "PhenoPET: a dedicated PET scanner for plant research based on digital SiPMs (DPCs)," in *IEEE Nuclear Science Symposium and Medical Imaging Conference (NSS/MIC)* (2014), p. 1.
71. P. Lopes, J. Bauer, A. Salomon, et al., "First in situ TOF-PET study using digital photon counters for proton range verification," Phys. Med. Biol. **61**, 6203 (2016).
72. J. F. Pratte, F. Nolet, S. Parent, et al., "3D photon-to-digital converter for radiation instrumentation: motivation and future works," Sensors **21**, 598 (2021).
73. B. Aull, E. Duerr, J. Frechette, et al., "Large-format geiger-mode avalanche photodiode arrays and readout circuits," IEEE J. Sel. Top. Quant. Electron. **24**, 3800510 (2018).
74. T. Mizuno, H. Ikeda, T. Nagano, et al., "Three-dimensional image sensor with MPPC for flash LIDAR," Trans. Jap. Soc. Aeron. Space Sci. **63**, 42 (2020).
75. A. Ximenes, P. Padmanabhan, M. Lee, et al., "A modular, direct time-of-flight depth sensor in 45/65-nm 3-D-stacked CMOS technology," IEEE J. Solid State Circ. **54**, 3203 (2019).
76. S. Hutchings, N. Johnston, I. Gyongy, et al., "A reconfigurable 3-D-stacked SPAD imager with in-pixel histogramming for flash LIDAR or high-speed time-of-flight imaging," IEEE J. Solid State Circ. **54**, 2947 (2019).
77. E. Conca, V. Sesta, M. Buttafava, et al., "Large-area, fast-gated digital SiPM with integrated TDC for portable and wearable time-domain NIRS," IEEE J. Solid State Circ. **55**, 3097 (2020).
78. N. D'Ascenzo, V. Saveliev, L. Wang, et al., "A digital photomultiplier device," Chinese Patent ZL201510397057.4 (2017-11-14).